Rapid Communications

Subharmonic spherical bubble oscillations induced by parametric surface modes

Matthieu Guédra,[1] Sarah Cleve,[2] Cyril Mauger,[2] and Claude Inserra[1,*]

[1]*Univ Lyon, Université Lyon 1, Centre Léon Bérard, INSERM, LabTAU, F-69003, LYON, France*

[2]*Univ Lyon, Ecole Centrale de Lyon, INSA Lyon, Université Claude Bernard Lyon I, CNRS, LMFA, UMR 5509, F-69134, ECULLY, France*

(Received 17 June 2019; published 27 January 2020)

A potential source of subharmonic bubble emissions is revealed experimentally by high-speed imaging. When an acoustic bubble is driven at sufficiently large pressure amplitudes, energy transfer from surface to volume oscillations can lead to the triggering of subharmonic spherical oscillations. This experimental evidence is in agreement with recent theoretical modeling of nonspherical bubble dynamics accounting for nonlinear mode coupling. Implications for the monitoring of stable cavitation activity are discussed.

DOI: 10.1103/PhysRevE.101.011101

I. INTRODUCTION

In sensitive therapeutic applications like blood-brain barrier opening by ultrasound, subharmonic (SH) emissions are a commonly used signature for quantifying the nonlinear oscillations of bubble clouds [1,2]. In this context, understanding the origin of SH emissions is crucial in the aim of differentiating stable and inertial cavitation regimes, as a strong interplay exists between them [3]. Amongst the identified sources, the predominant hypothesis is that bubbles whose radii are close to twice the resonant radius will promote subharmonic oscillation as expected by single bubble [4] and interacting bubble cloud [5] theories. Other causes for subharmonic emissions are (i) the periodic collapse of collective bubbles [6], (ii) the strongly nonlinear oscillations (routing to chaos) of bubbles with near-resonant radii [7], and (iii) the onset of surface modes through parametric excitation [8]. Considering the last origin, its main drawback to explain experimental observations is the weak radiative efficiency of the nonspherical oscillations on their own [9]. However, when nonspherical oscillations arise, several shape modes can be excited simultaneously with the possibility of nonlinear mode mixing [10]. Particularly, a *surface-to-volume* energy transfer has been theoretically demonstrated through nonlinear mode coupling up to the third order [11,12]. Because a given shape mode excited on the first parametric resonance would oscillate at half the fundamental frequency, the existence of nonlinear energy transfer in the equation ruling the spherical bubble oscillation could possibly lead to the enhancement of subharmonic spherical oscillations. To our knowledge this case was only investigated theoretically so far [9,13,14].

In this Rapid Communication, we investigate experimentally the triggering of subharmonic spherical oscillations that results from surface-to-volume energy transfer. We present high-speed imaging of bubble temporal dynamics to confirm that the appearance of subharmonic spherical emissions is correlated to the onset of surface oscillations. These temporal dynamics are successfully compared to numerical simulations that correctly predict both the onset and finite amplitude of the SH emission. The role of nonlinear mode coupling on this energy transfer is highlighted.

II. EXPERIMENTAL SETUP

Extensive details about the experimental setup [Fig. 1(a)] can be found in previous works [10,15]. Briefly, single laser-nucleated air bubbles of few tens of micrometers in radius are trapped in a cubic tank of distilled undegassed water. Trapping occurs at pressure antinodes of a standing-wave ultrasound field ($f_a = 31.25$ kHz) since considered bubbles lie below the resonant radius ($\sim$110 μm). In order to allow investigation of shape oscillations by limiting diverging amplitude growth, surface instabilities are periodically triggered on short time periods by driving bubbles in a slowly varying amplitude-modulated acoustic pressure field of the form $p_a(t) = P_a \cos(2\pi f_a t)[1 - \eta \cos(2\pi f_m t)]$, where P_a is the mean pressure amplitude, $f_m \ll f_a$ is the low modulation frequency ($f_a/f_m = 400$), and η is the modulation amplitude. To fully capture the bubble dynamics and ensure a proper analysis of the nonspherical deviation of the bubble interface, an optical setup composed of two orthogonal and synchronous high-speed cameras (Vision Research, Phantom V12.1) is used. High-speed imaging is undertaken at 180×10^3 frames per second (frame size 128×128 pixels) and the bubble contour determining the surface coordinate $r_s(\theta, t)$ is obtained from backlit illumination using continuous light sources. Expanding this contour on the Legendre polynomial basis $r_s(\theta, t) = \sum_{n=0}^{N} a_n(t) P_n(\cos\theta)$ leads to the quantification of the volume (a_0), translational (a_1), and nonspherical (a_n, $n \geqslant 2$) mode amplitudes.

The multiview capture is used to perfectly define the spatial orientation of the bubble, particularly the correct angle formed between the axis of symmetry of the deformed shape (here denoted as $\mathbf{e_b}$) and the vertical $\mathbf{e_z}$ axis shared by both cameras [Fig. 1(b)]. Different possibilities for inappropriate orientation of the bubble leading to discrepancy between the captured apparent contour and the real nonspherical deformation are discussed in detail in Ref. [15]. Figure 1(b) illustrates one particular bubble orientation where the $\mathbf{e_b}$ axis lies in the

*claude.inserra@inserm.fr

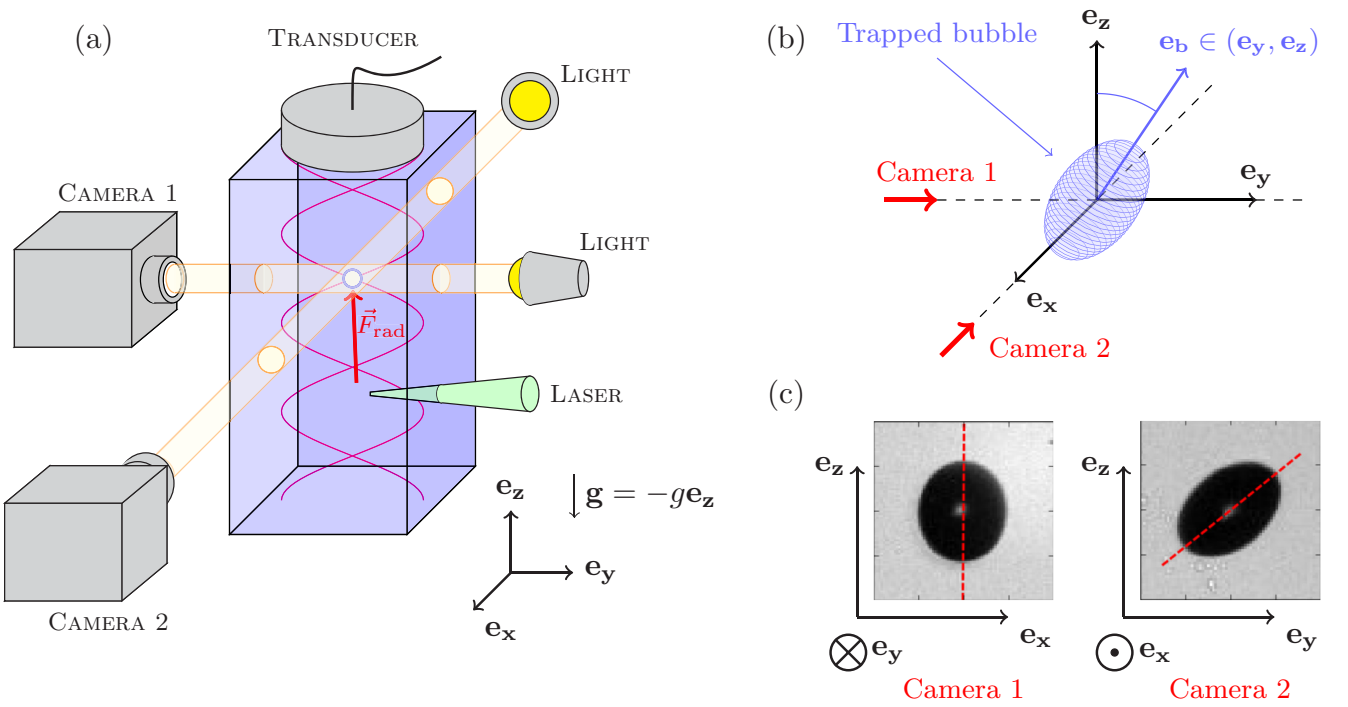

FIG. 1. (a) Schematic representation of the experimental setup. (b) Orientation of the trapped bubble. The axis of symmetry of the bubble is identified by the unit vector $\mathbf{e_b}$. (c) Associated side views of the bubble on both cameras. The bubble is oriented as in (b).

$(\mathbf{e_y}, \mathbf{e_z})$ plane corresponding to the view plane captured by the second camera. In this case, only the recordings from the second camera lead to a correct modal decomposition of the bubble contour, while the first camera captures artificial surface oscillations that in fact come from the combination of all vibration modes [Fig. 1(c)]. The results presented in this Rapid Communication are obtained from the modal decomposition of the bubble surface captured by the second camera.

III. RESULTS

Figure 2(a) depicts the bubble temporal dynamics over one single low-frequency modulation period, for a bubble of radius $R_0 = 43.8$ μm driven at mean acoustic amplitude $P_a = 22.5$ kPa and modulation amplitude $\eta = 0.23$. To describe which nonspherical oscillations are expected, we recall that surface oscillations result from a parametric instability. For the given angular forcing frequency $\omega_a = 2\pi f_a$, a shape oscillation will be triggered if the bubble radius is close to the resonant radius of a mode n following the spectrum of shape mode eigenfrequencies [16]:

$$\omega_n^2 = (n-1)(n+1)(n+2)\sigma/\rho R_0^3, \tag{1}$$

where σ is the surface tension and ρ is the density of the liquid. In our experiment the angular frequency ω_a is fixed, therefore a nonspherical mode 2 may appear on its first parametric resonance ($\omega_n = \omega_a/2$) if the bubble radius is close to 44 μm [following Eq. (1)]. In consequence the bubble radius $R_0 = 43.8$ μm may predominantly lead to the excitation of a nonspherical mode 2. Only the spherical (a_0) and the dominant nonspherical oscillations (a_2, a_4) are shown in Fig. 2, while translational (a_1) and third (a_3) modes are omitted because of negligible amplitude compared to the others ($|a_{1,3}| < 0.5$ μm). We take advantage of the long-time periodicity of the onset of nonspherical oscillations during successive modulation periods [10] in order to increase the time resolution from a stroboscopic recombination of the whole temporal signal within one single low-frequency modulation period as the one presented in Fig. 2(a).

The predominant second shape mode is triggered when the applied acoustic pressure reaches the critical pressure threshold leading to the parametric instability [8]. This threshold is estimated to $P_{2,\text{th}} \simeq 18.1$ kPa in the vicinity of the first parametric resonance, indeed lower than the applied acoustic pressure used in this experiment. After an exponential growth and saturation to a plateau, a slow decay occurs as the applied acoustic pressure decreases to less than $P_{2,\text{th}}$. The time-resolved dynamics of the spherical and dominant nonspherical oscillations is shown in Fig. 2(b) over a dozen acoustic periods. Looking at the precise temporal dynamics at the acoustic timescale reveals that the second shape mode oscillates mainly at half the ultrasound frequency $f_a/2$, as expected for a first parametric resonance excitation. This frequency content is illustrated in Fig. 2(c) which displays the computed Fourier coefficients $c(f)$ of the volume and surface oscillations taken roughly at the middle of the modulation period. Figure 2(a) also highlights the appearance of the fourth shape mode (a_4), although its theoretical parametric threshold is estimated to $P_{4,\text{th}} \simeq 37$ kPa. This additional mode, mainly oscillating at the driving frequency f_a [Figs. 2(b) and 2(c)], is known to emerge from nonlinear mode coupling [10]. More precisely, its origin lies in the quadratic contributions of the second mode a_2 to the dynamics of the fourth mode a_4. Finally, investigating in detail the frequency content of the volume and nonspherical

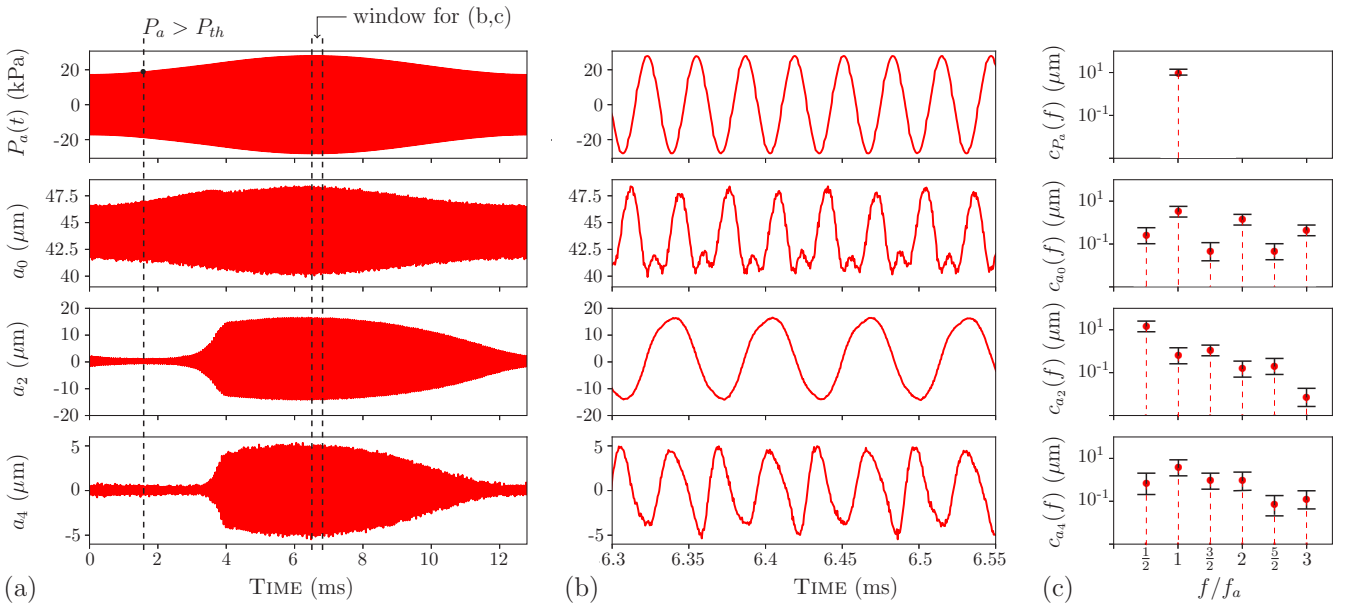

FIG. 2. (a) Temporal evolution of the applied acoustic pressure, the volume, and dominant ($n = 2, 4$) surface modes onto a single low-frequency modulation period. The bubble of radius $R_0 = 43.8$ μm is driven at the mean acoustic amplitude $P_a = 22.5$ kPa and modulation amplitude $\eta = 0.23$. (b) Temporal evolution of the same components as in (a) when zooming on eight acoustic periods, for the time signal windowed at half the modulation period, as illustrated in (a). (c) Fourier coefficients $c(f)$ of the applied acoustic pressure, the volume, and (a_2, a_4) modes for the same time interval as (b). Average ± standard deviation ($n = 10$). Error bars are calculated by using the modal amplitudes of the considered nonspherical modes, measured over ten successive modulation periods, at the same time after the onset of the predominant shape mode.

modes shown in Fig. 2(c) reveals (i) the nonlinear behavior of nonspherical oscillations, exhibiting harmonic (for mode 2) and subharmonic (for mode 4) behaviors and (ii) the presence of a SH component in the spherical (volumic) oscillations. This SH component in the breathing (volumic) oscillation is clearly visible in Fig. 2(b).

A. Triggering of SH emissions

Considering the classical sources of volumic SH emissions for the presented case ($R_0 = 43.8$ μm, $P_a = 22.5$ kPa) allows stating that (i) this bubble is small compared to twice the resonant size ($R_0/R_{\text{res}} \sim 0.4$) and (ii) the applied acoustic pressure is lower than the one required to enhance volumic *route-to-chaos* SH emissions. Indeed, solving the standard Keller-Miksis equation for purely spherical oscillations leads to an estimate of the SH emission threshold $P_{\text{SH}} \simeq 86$ kPa. For an acoustic pressure much lower than this value, the observed SH oscillations should be induced by the presence of surface oscillations. In order to confirm this hypothesis, Fig. 3(a) presents the evolution of the Fourier coefficients over the entire modulation period, $c_{a_0}[1/2]$, corresponding to the subharmonic component of the spherical oscillation $R(t)$, and $c_{a_2}[1/2]$ corresponding to the parametric component of the ellipsoidal shape mode $a_2(t)$. These results show that the SH amplitude follows the same temporal dynamics as the dominant surface mode, characterized by an exponential growth, a saturation, and a slow decay. Subharmonic oscillations clearly occur once the onset of surface modes is reached. In the following, these experimental findings are strengthened by numerical simulations.

B. Numerical simulations

To capture the appearance of volumic SH oscillations, we consider a mathematical formulation accounting for nonlinear interactions between volume oscillations, translation, and shape deformations of the bubble [11]. This model already demonstrated its ability to recover the experimental observations made on nonlinear surface oscillations such as saturation of the instability and appearance of nonparametric shape modes [10]. Limited to second-order accuracy and simplified by assuming (i) uniform incident acoustic pressure, (ii) negligible translational motion, and (iii) boundary layer approximation for viscous dissipation, the theory reduces to the following set of differential equations governing the spherical a_0 and nonspherical $a_n (n \geqslant 2)$ modal amplitudes:

$$a_0\ddot{a}_0 + \frac{3}{2}\dot{a}_0{}^2 = \frac{1}{\rho}\left(p_\infty + \frac{2\sigma}{R_0}\right)\left(\frac{R_0}{a_0}\right)^{3\gamma} - \frac{p_\infty + p_a(t)}{\rho} - \frac{2\sigma}{\rho a_0} - 4\nu\frac{\dot{a}_0}{a_0} + \epsilon^2 h_0\left(a_i^2, \dot{a}_i{}^2, a_i\dot{a}_i\right), \quad (2)$$

$$\ddot{a}_n + B_n\dot{a}_n - A_n a_n = \epsilon h_n\left(a_i^2, \dot{a}_i{}^2, a_i\dot{a}_i, a_i a_j, a_i\dot{a}_j\right), \quad (3)$$

where ρ and ν are the liquid density and kinematic viscosity, σ is the surface tension, γ is the gas polytropic index, p_∞ and $p_a(t)$ are the static and acoustic components of the liquid pressure, and the quantities A_n and B_n are time-varying coefficients whose expressions can be found

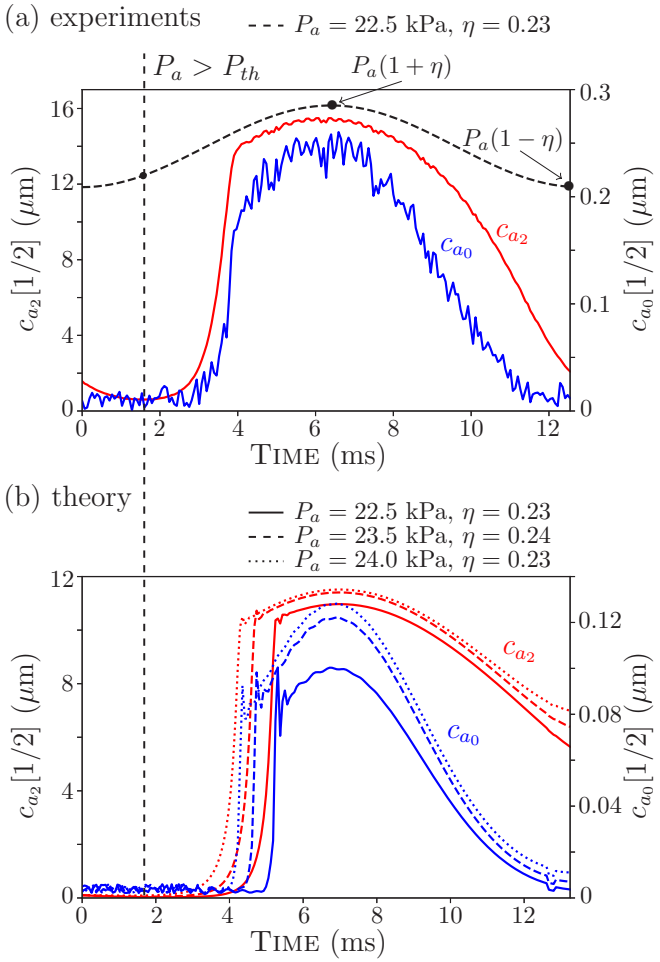

FIG. 3. Temporal evolution of the Fourier coefficients c_{a_0} of the subharmonic component of the spherical oscillation $a_0(t)$ and c_{a_2} of the surface mode $a_2(t)$. Results are shown over a single modulation period. (a) Experimental results. The low-frequency envelope of the acoustic field is depicted by a dashed line. (b) Theoretical results from the modeling accounting for nonlinear mode coupling. The different curves in continuous, dashed, or dotted lines are obtained for different pairs of variables (P_a, η).

in Ref. [8]. The functions h_0 and h_n take into account the nonlinear interactions between the surface modes; their mathematical expressions are derived in Ref. [11]. Performing the numerical integration of Eqs. (2) and (3) applying the experimental conditions $R_0 = 43.8$ μm, $P_a = 22.5$ kPa, and $\eta = 0.23$ allows recovering the temporal dynamics of the spherical, second mode a_2 and fourth mode a_4 similarly to the experimental results presented in Fig. 2(a) over a single modulation period. These dynamics are not shown in the present Rapid Communication. We rather focus here on the volumic SH emission by presenting in Fig. 3(b) the Fourier coefficients $c_{a_0}(t)$ and $c_{a_2}(t)$ computed from the simulation over a modulation period. It is worth noting that the volumic SH appearance and its global dynamics are well captured by the model, even if a difference remains concerning the amplitude of the oscillations. In particular, the onset of SH emission is well correlated to the onset of the parametrically excited surface mode a_2, as observed experimentally in Fig. 3(a). In addition, the origin of the SH emission lies in the intrinsic nonlinear features of the nonspherical oscillations. Indeed, the interaction term $h_0(a_i^2, \dot{a}_i{}^2, a_i\dot{a}_i)$ responsible for the surface-to-volume energy transfer in Eq. (2) does not involve either linear terms a_i or cross products $a_i a_j$ $(i \neq j)$, thus avoiding the direct excitation of volumic SH oscillations from the natural frequency content of first parametrically excited (oscillating at $f_a/2$) and nonlinearly triggered (f_a) surface modes. The SH component can therefore solely appear from the nonlinear frequency characteristics of each generated surface mode. At first, to obtain even stronger SH spherical emission, the amplitudes of nonspherical oscillations can be increased. Numerical results obtained for the couple of parameters ($P_a = 23.5$ kPa, $\eta = 0.24$) and ($P_a = 24$ kPa, $\eta = 0.23$) are shown in Fig. 3(b). While the amplitude of the c_{a_2} coefficient changes slightly and saturates to a limit value, the component c_{a_0} of the subharmonic spherical component increases. Still its maximum value does not exceed half that of the experimental case. Increasing the nonspherical oscillation amplitudes seems not sufficient to alleviate the observed discrepancy. Although globally consistent with the experimental results, an even better agreement would require numerical simulations with modeling expanded to the cubic order, as the one derived by Shaw [11], here reduced to the second order for simplicity.

IV. CONCLUSIONS

SH emissions induced by nonspherical oscillations occurring at half the fundamental frequency are usually disregarded as a possible cause of SH emissions of a bubble cloud as the radiation efficiency of the half-frequency emitted component decays with the distance as $r^{-(n+1)}$ and the mode number n [9]. Here, we clearly demonstrate that surface mode oscillations could also lead to the appearance of a SH component in the volumic oscillation of the bubble through nonlinear mode coupling. This SH oscillation thus leads to a monopole radiation of sound, possibly detected even at moderate distances depending on the amplitude of the generated SH oscillation. To estimate how strong the SH emission induced by the revealed mechanism is, the radiated acoustic pressure $P_{\text{rad}} = \rho(a_0^2\ddot{a}_0 + 2a_0\dot{a}_0{}^2)$ (at a distance $D = 1$ m) can be computed from the Fourier series expansion of $a_0(t)$ used to determine the Fourier coefficients given in Fig. 2. Computing the frequency spectrum of the radiated pressure reveals a subharmonic component ($f_a/2$) amplitude 35 dB lower than the fundamental. This ratio allows expecting experimental observations of the emitted SH emission originated from this mechanism, and lies in the $[-40, -20]$ dB ratio commonly used to numerically estimate the subharmonic threshold [3] and encountered in experimental conditions [1,17]. Therefore, it can be assumed that this mechanism brings noticeable contributions to SH emissions of bubble clouds when monitored for limiting side effects in sensitive therapeutic applications [2]. We report a SH emission originated from a stably (temporally) oscillating bubble with nonspherical shape that contributes uniquely to stable cavitation activity. Although shape instabilities are usually considered as a bubble breakup precursor (inertial activity), surface modes can also be easily obtained when radial motion and surface oscillations

are in near resonance [7]. When insonifying a polydisperse bubble cloud at a given ultrasound frequency, multiple resonances of surface modes could occur for a wide range of bubble radii. This implies additional contributions to SH emissions of bubble radii different from twice the resonance radius.

ACKNOWLEDGMENTS

This work was supported by the French National Research Agency ANR-MOST project CARIBBBOU (ANR-15-CE19-0003) and the LabEx CeLyA of the University of Lyon (ANR-10-LABX-0060/ANR-11-IDEX-0007).

[1] C. H. Tsai, J. W. Zhang, Y. Y. Liao, and H. L. Liu, Real-time monitoring of focused ultrasound blood-brain barrier opening via subharmonic acoustic emission detection: Implementation of confocal dual-frequency piezoelectric transducers, Phys. Med. Biol. **61**, 2926 (2016).

[2] M. A. O'Reilly and K. Hynynen, Blood-brain barrier: Real-time feedback-controlled focused ultrasound disruption by using an acoustic emission-based controller, Radiology **263**, 96 (2012).

[3] K. B. Bader and C. K. Holland, Gauging the likelihood of stable cavitation from ultrasound contrast agents, Phys. Med. Biol. **58**, 127 (2013).

[4] A. Prosperetti, A general derivation of the subharmonic threshold for nonlinear bubble oscillations, J. Acoust. Soc. Am. **133**, 3719 (2013).

[5] M. Guédra, C. Cornu, and C. Inserra, A derivation of the cavitation threshold accounting for bubble-bubble interactions, Ultrason. Sonochem. **38**, 168 (2017).

[6] K. Johnston, C. Tapia-Siles, B. Gerold, M. Postema, S. Cochran, A. Cuschieri, and P. Prentice, Periodic shock-emission from acoustically driven cavitation clouds: A source of the subharmonic signal, Ultrasonics **54**, 2151 (2014).

[7] W. Lauterborn and T. Kurz, Physics of bubble oscillations, Rep. Prog. Phys. **73**, 106501 (2010).

[8] M. P. Brenner, D. Lohse, and T. F. Dupont, Bubble Shape Oscillations and the Onset of Sonoluminescence, Phys. Rev. Lett. **75**, 954 (1995).

[9] M. S. Longuet-Higgins, Monopole emission of sound by asymmetric bubble oscillations. Part 1. Normal modes, J. Fluid Mech. **201**, 525 (1989).

[10] M. Guédra, C. Inserra, C. Mauger, and B. Gilles, Experimental evidence of nonlinear mode coupling between spherical and nonspherical oscillations of microbubbles, Phys. Rev. E **94**, 053115 (2016).

[11] S. J. Shaw, Translation and oscillation of a bubble under axisymmetric deformation, Phys. Fluids **18**, 072104 (2006).

[12] S. J. Shaw, The stability of a bubble in a weakly viscous liquid subject to an acoustic traveling wave, Phys. Fluids **21**, 022104 (2009).

[13] C. C. Mei and X. Zhou, Parametric resonance of a spherical bubble, J. Fluid Mech. **229**, 29 (1991).

[14] S. J. Shaw, Nonspherical sub-millimeter gas bubble oscillations: Parametric forcing and nonlinear shape mode coupling, Phys. Fluids **29**, 122103 (2017).

[15] M. Guédra, S. Cleve, C. Mauger, P. Blanc-Benon, and C. Inserra, Dynamics of nonspherical microbubble oscillations above instability threshold, Phys. Rev. E **96**, 063104 (2017).

[16] H. Lamb, *Hydrodynamics*, 6th ed. (Cambridge University Press, Cambridge, 2017).

[17] G. A. Husseini, M. A. Diaz de la Rosa, E. S. Richardson, D. A. Christensen, and W. G. Pitt, The role of cavitation in acoustically activated drug delivery, J. Control. Release **107**, 253 (2005).